ACS NANO

www.acsnano.org

ARTICLE

Petal-like MoS_2 Nanosheets Space-Confined in Hollow Mesoporous Carbon Spheres for Enhanced Lithium Storage Performance

Xiue Zhang,[†] Rongfang Zhao,[†] Qianhui Wu,[†] Wenlong Li,[†] Chao Shen,[†] Lubin Ni,[†] Hui Yan,[‡] Guowang Diao,*[,†] and Ming Chen*[,†]

[†]School of Chemistry and Chemical Engineering, Yangzhou University, Yangzhou, Jiangsu 225002, China

[‡]Department of Chemistry, University of Louisiana at Lafayette, Lafayette, Louisiana 70504, United States

Supporting Information

ABSTRACT: **An innovative approach for efficient synthesis of petal-like molybdenum disulfide nanosheets inside hollow mesoporous carbon spheres (HMCSs), the yolk−shell structured MoS_2@C, has been developed. HMCSs effectively control and confine *in situ* growth of MoS_2 nanosheets and significantly improve the conductivity and structural stability of the hybrid material. The yolk−shell structured MoS_2@C is proven to achieve high reversible capacity (993 mA h g^{-1} at 1 A g^{-1} after 200 cycles), superior rate capability (595 mA h g^{-1} at a current density of 10 A g^{-1}), and excellent cycle performance (962 mA h g^{-1} at 1 A g^{-1} after 1000 cycles and 624 mA h g^{-1} at 5 A g^{-1} after 400 cycles) when evaluated as an anode material for lithium-ion batteries. This superior performance is attributed to the yolk−shell structure with conductive mesoporous carbon as the shell and the stack of two-dimensional MoS_2 nanosheets as the yolk.**

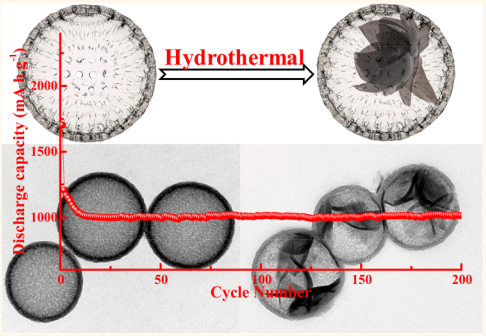

KEYWORDS: *yolk−shell structured MoS_2@C, hollow mesoporous carbon spheres, in situ confined growth, enhanced electrochemistry performance, lithium-ion batteries*

As an architecture of functional materials, the yolk−shell nanostructure has been extensively studied in recent years.[1−4] Research has shown that yolk−shell structured materials with the controlled tuning of both cores and hollow shells provide powerful applications in catalysis,[5,6] controlled drug release,[7,8] medical imaging,[9] energy conversion, and storage.[10,11] In particular, the core of yolk−shell structured nanomaterials enhances the energy density of lithium-ion batteries (LIBs) by increasing the weight fraction of the electrochemical active component.[12] Furthermore, the void between the yolk and the shell can serve as a buffering zone for the free volume expansion of electroactive core material during lithium insertion/extraction.[10] Therefore, uniform, size-controllable, and well-defined yolk−shell structured nanomaterials have been synthesized and studied as electrode materials.[13−19] Among various preparation methods, the selective etching or dissolution template methods have been generally accepted for the production of yolk−shell structured powders.[13,18,19] However, the multistep synthetic process and the partial collapse of hollow shell in the template removal process limit the application of the approach. Therefore, it is highly desired to develop a facile and more effective strategy for synthesizing yolk−shell structured nanomaterials.

Molybdenum disulfide (MoS_2), as a representative two-dimensional (2D) material, has received extensive attention owing to its tunable structures and Li^+ storage performance in LIBs. The theoretical capacity of MoS_2 (~670 mA h g^{-1}) is almost double that of graphite anodes (~370 mA h g^{-1}). However, the rapid degradation of capacity and poor rate performance greatly restrict the application of MoS_2. Thus, many methods have been proposed to enhance the electrochemical property of MoS_2 by coating carbonaceous materials, transforming the micro-nano structure, or increasing the interlayer distance of MoS_2.[20−34] The carbon coating has been one of the most effective and straightforward strategies to enhance the electrochemical property.[20−32] Several structures of MoS_2 supported on carbonaceous materials have been synthesized; nevertheless, to the best of our knowledge, the yolk−shell structured MoS_2@C obtained by using a "ship-in-a-bottle" strategy has not been reported.

Herein, we have developed an innovative approach to synthesize MoS_2 nanosheets inside hollow mesoporous carbon spheres (HMCSs). HMCSs serve as nanoreactors and can

Received: June 12, 2017
Accepted: July 25, 2017
Published: July 25, 2017

DOI: 10.1021/acsnano.7b04078
ACS Nano 2017, 11, 8429−8436

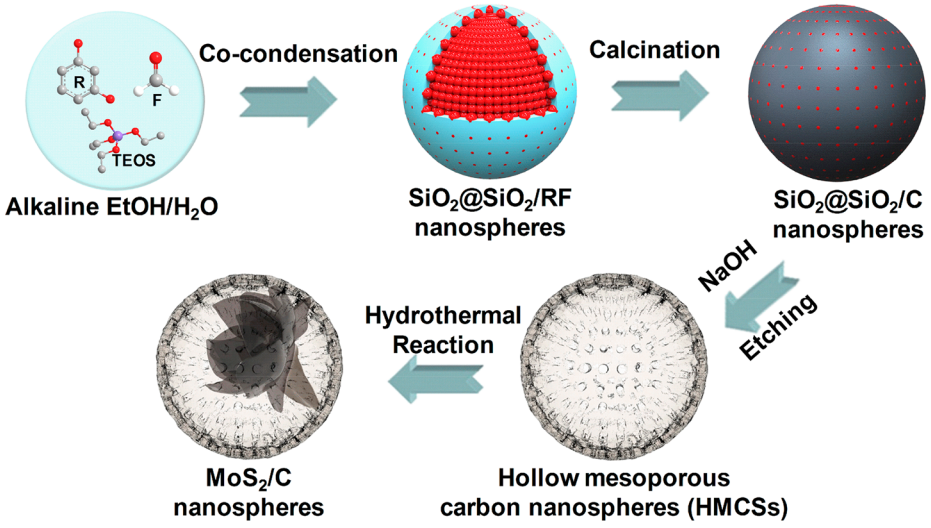

Figure 1. Mechanism for the development of the yolk–shell MoS_2@C nanospheres.

control the confined growth of MoS_2 nanosheets. When evaluated as an anode material for LIBs, the yolk–shell structured MoS_2@C shows higher reversible capacity and better rate capability, compared to that of pure MoS_2 and MoS_2 supported on carbon spheres (C@MoS_2).

RESULTS AND DISCUSSION

Characterization of Yolk–Shell MoS_2@C Nanospheres. The strategy for synthesizing the yolk–shell MoS_2@C nanospheres is illustrated in Figure 1. First, tetraethylorthosilicate (TEOS) and resorcinol formaldehyde (RF) oligomers are co-condensed on SiO_2 core particles to form the SiO_2@SiO_2/RF core–shell structured nanospheres with a uniform average size of 320 ± 30 nm (Figure S1a,c in the Supporting Information). Second, SiO_2@SiO_2/RF is converted into SiO_2@SiO_2/C after calcination in N_2 (Figure S1b,d). Third, SiO_2 is easily removed by NaOH to obtain hollow mesoporous carbon spheres (HMCSs).[35,36] Last, followed by a facile hydrothermal method, MoS_2 nanosheets successfully grow in the cavity of the HMCSs.

Transmission electron microscopy (TEM) and field-emission scanning electron microscopy (FESEM) were used to investigate the morphologies of HMCSs and MoS_2@C nanospheres. The carbon nanospheres with hollow structure are uniform and consist of many disorderly pores on the carbon shells. The shells are ~20 nm thick and envelop a large void of diameter of ~300 nm, as shown in Figure 2a–c. The Brunauer–Emmett–Teller (BET) analysis shows that the specific surface area of HMCSs is about 770.7 m^2 g^{-1}, and the main pore size is about 2.1 nm in diameter (Figure S2a,b). After the hydrothermal process, the petal-like MoS_2 nanosheets grew in the hollow cavity of HMCSs to form the yolk–shell MoS_2@C nanospheres, and the porous carbon shell remains intact (Figure 2d–f). The corresponding FESEM images (Figure S3) clearly show a uniform distribution of particle size and good dispersibility of the yolk–shell MoS_2@C nanospheres. The selected area electron diffraction (SAED) pattern (Figure 2i) of the yolk–shell MoS_2@C nanospheres shows the Debye–Scherrer ring patterns of (002), (101), (103), and (008), which can be indexed with the standard hexagonal MoS_2,[37] suggesting the synthesized yolk–shell MoS_2@C nanospheres are polycrystals. The high-resolution

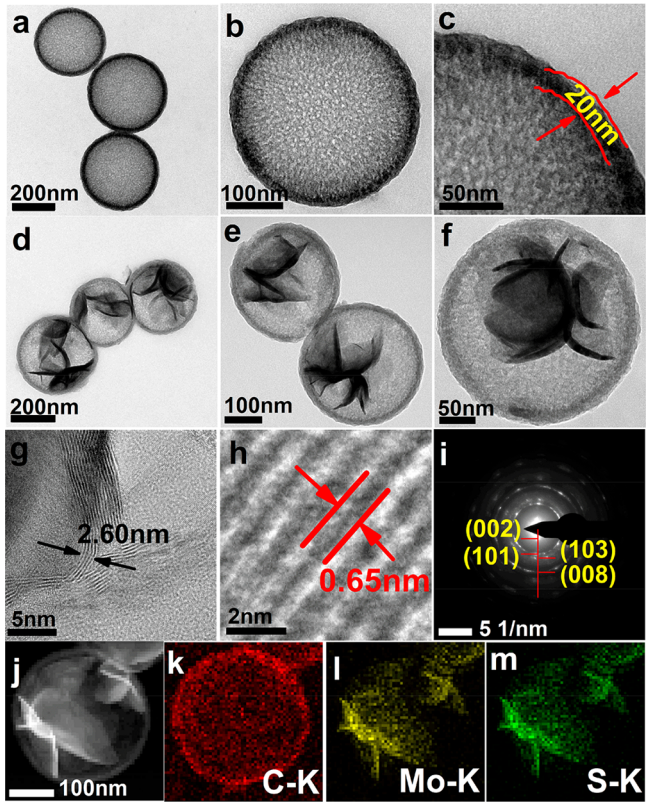

Figure 2. (a–c) TEM images of the HMCSs; (d–f) TEM images, (g,h) HRTEM images, and (i) SAED pattern of MoS_2@C nanospheres; (j–m) annular dark-field STEM image and the corresponding EDX elemental mappings of C, Mo, and S in a single MoS_2@C nanosphere.

TEM (HRTEM) image of the yolk–shell MoS_2@C nanospheres clearly demonstrates that the layers of MoS_2 nanosheets range from three to nine layers (Figure 2g). The interplanar distance of the MoS_2 nanosheets is measured to be about 0.65 nm, corresponding to the *d*-spacing of (002) planes of hexagonal MoS_2 (Figure 2h).[21,24] The yolk–shell structure of MoS_2@C nanospheres is further supported by the elemental mapping from energy-dispersive X-ray (EDX) spectroscopy with the annular dark-field STEM. EDX mappings of a single

DOI: 10.1021/acsnano.7b04078
ACS Nano 2017, 11, 8429–8436

nanosphere show the presence and distribution of C, Mo, and S elements (Figure 2k–m). It is obvious that the petal-like MoS_2 nanosheets are located inside HMCSs. The weight fraction of MoS_2 in MoS_2@C nanospheres is 77.8 wt % obtained from thermal gravity analysis (TGA) of pure MoS_2 nanosheets and MoS_2@C nanospheres (Figure S4). The BET analysis shows that the specific surface area of the MoS_2@C nanospheres is 199.2 $m^2\ g^{-1}$ (Figure S5), which is larger than that of C@MoS_2 nanoboxes (123.7 $m^2\ g^{-1}$).[20]

C@MoS_2 nanospheres and pure MoS_2 nanosheets, as reference materials, were prepared with a similar hydrothermal method. The synthesis scheme of C@MoS_2 nanospheres is illustrated in Figure S6. FESEM and TEM images of C@MoS_2 nanospheres and pure MoS_2 nanosheets are shown in Figure S7 and Figure S8, respectively. The X-ray photoelectron spectroscopy (XPS) confirms the composition of C@MoS_2 (Figure S9). The C@MoS_2 nanospheres have 83.4 wt % MoS_2 according to TGA of pure MoS_2 nanosheets and C@MoS_2 nanospheres (Figure S10). The specific surface area of C@MoS_2 nanospheres is about 44.4 $m^2\ g^{-1}$ obtained by BET analysis (Figure S11), which is smaller than that of the MoS_2@C nanospheres.

The XRD patterns of pure MoS_2, C@MoS_2, and MoS_2@C in Figure 3a match the hexagonal crystal structure of MoS_2

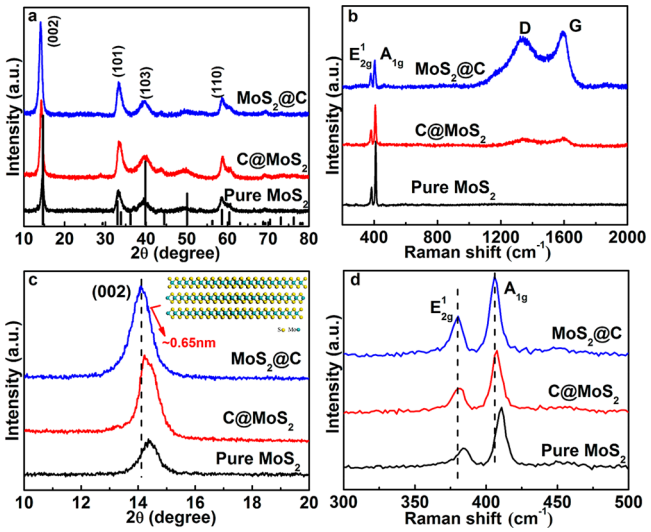

Figure 3. (a) XRD pattern, (b) Raman spectra, (c) XRD pattern of the (002) plane peak, and (d) Raman spectra of $^1E_{2g}$ and A_{1g} vibration modes of pure MoS_2, C@MoS_2, and MoS_2@C nanospheres.

(JCPDS card no. 37-1492). However, the distinct diffraction peak of the (002) crystalline plane of yolk–shell MoS_2@C shifts to a lower angle (14.1°), compared to that of pure MoS_2 (14.4°) (Figure 3c), suggesting an increased interlayer distance of the (002) plane, and this is consistent with the result from the HRTEM image (Figure 2h), where the *d* of the (002) plane increased from 0.62 to 0.65 nm. Raman spectra further confirm the existence of hexagonal MoS_2 nanosheets in HMCSs (Figure 3b). For pure MoS_2, the two distinct Raman peaks at 384.1 and 411.2 cm^{-1} are ascribed to the typical $^1E_{2g}$ and A_{1g} vibration modes of the hexagonal MoS_2 crystal,[28,30] respectively. In yolk–shell MoS_2@C nanospheres, the above two peaks are shifted to 380.7 and 405.1 cm^{-1}. It has been reported that the frequency difference between the $^1E_{2g}$ and A_{1g} vibration modes decreases stepwise with the decreasing number of MoS_2 layers. In this case, the frequency differences for pure MoS_2, C@MoS_2, and MoS_2@C are 27.1, 26.5, and 24.4 cm^{-1}, respectively, indicating that the MoS_2 nanosheets as the yolk in yolk–shell MoS_2@C have the least number of MoS_2 layers among them (Figure 3d). In Figure 3b, the other two peaks located at 1340 and 1591 cm^{-1} in MoS_2@C nanospheres are attributed to the D and G bands of carbon, which confirms the presence of the carbon shell. Compared with that of C@MoS_2, the intensity of D and G bands in MoS_2@C is higher, indicating the structure difference between MoS_2@C and C@MoS_2. XPS of yolk–shell MoS_2@C nanospheres shows the atomic ratio of Mo to S is close to 2.0, matching the stoichiometry value of MoS_2. The C 1s peaks at 284.7, 286.2, and 287.4 eV are ascribed to C–C, C–O, and C═O, respectively (Figure 4b). The Mo 3d spectra

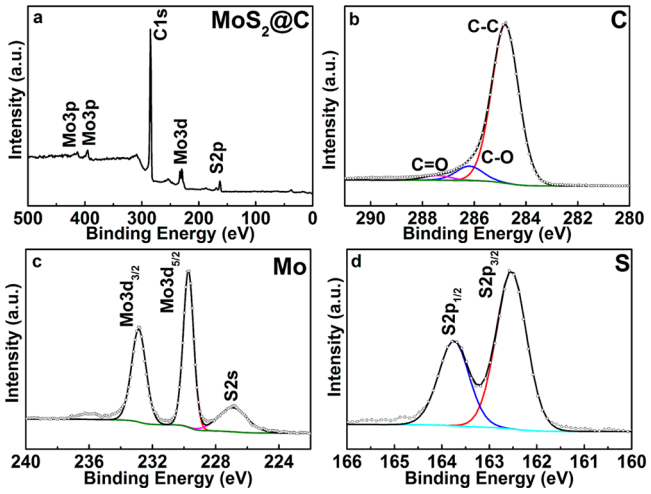

Figure 4. (a) XPS of MoS_2@C nanosphere survey spectrum and (b–d) high-resolution spectra of C 1s, Mo 3d, and S 2p.

show two peaks at 229.7 and 232.8 eV, assigned to Mo $3d_{5/2}$ and Mo $3d_{3/2}$, respectively, indicating the existence of Mo^{4+} (Figure 4c).[21,33] Two peaks at 162.5 and 163.7 eV in the S 2p spectrum are from the spin–orbit doublet of S $2p_{3/2}$ and S $2p_{1/2}$, respectively (Figure 4d).

The growth mechanism of yolk–shell MoS_2@C nanospheres is discussed. Adding NH_2CSNH_2 to the system, under hydrothermal conditions, releases H_2S gas through the reaction of $NH_2CSNH_2 + 2H_2O \rightarrow 2NH_3 + H_2S + CO_2$.[38] H_2S gas tends to adsorb on the rough porous carbon inner wall, leading to a high concentration of H_2S in the cavity of HMCSs. Subsequently, combined with the other high concentration reactants such as MoO_4^{2-}, the MoS_2 nucleates inside HMCSs. Because the reactants can freely diffuse into the hollow cavity of HMCSs *via* the mesoporous shell, the confined growth of MoS_2 in the HMCS nanoreactor is further achieved after the nucleation. Obviously, in this approach, the HMCSs play crucial roles by both providing nucleation sites on the carbon shells and confining the growing region of MoS_2 during the hydrothermal process. Without mesoporous pores on the carbon shell, MoS_2 will directly grow on carbon shells.[20,27,28] The TEM images of MoS_2@C nanospheres, acquired at different reaction times, show the growth evolution of MoS_2 from smaller and fewer nanosheets to self-assembled petal-like structure (Figure 5). This detailed time course study confirms that MoS_2 nucleates on porous carbon inner wall of HMCSs, and the growth of MoS_2 is confined to the HMCSs'

DOI: 10.1021/acsnano.7b04078
ACS Nano 2017, 11, 8429–8436

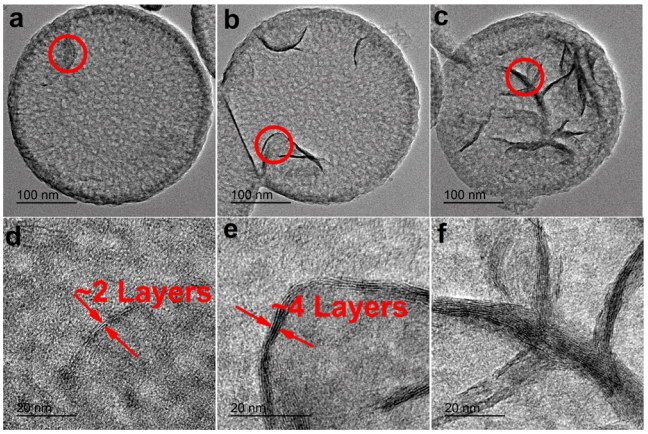

Figure 5. TEM images of MoS_2@C at reaction time of (a,d) 2 h, (b,e) 5 h, and (c,f) 8 h, during the hydrothermal reaction.

nanoreactor. In addition, the effect of the thickness of the carbon shell on the structure of nanospheres further suggests that the nucleation is a competitive process between inside cavity and outside shell of HMCSs. When the thickness of the carbon shell is increased to 65 nm, the MoS_2 layers grow not only on the inner wall but also on the outside surface of HMCSs (Figure S12). The thicker carbon shell limits the ion diffusion and migration, resulting in the competitive growth on both the inside and the outside of the carbon shell, though the 65 nm and the 20 nm shells have the same distribution of pore size (Figure S2b,d). It is particularly gratifying that this method can be applied to the synthesis of other yolk–shell metal dichalcogenide@C nanospheres, such as WS_2@C (Figure S13) and SnS_2@C (Figure S14).

Electrochemical Performance of Yolk–Shell MoS_2@C Nanospheres. The lithium storage properties of yolk–shell MoS_2@C nanospheres are evaluated using cyclic voltammetry (CV) (Figure 6a). In the first negative scan, the first cathodic peak at 1.10 V is related to the intercalation of Li^+ into the MoS_2 lattice accompanied by the formation of Li_xMoS_2. The second cathodic peak at about 0.44 V corresponds to the subsequent conversion reaction: $Li_xMoS_2 + (4-x)Li^+ + (4-x)e^- \rightarrow Mo + 2Li_2S$.[22,39,40] In the reverse scan, a very weak anodic peak at 1.72 V is due to the incomplete oxidation of Mo metal, and another pronounced peak at 2.27 V can be attributed to the delithiation of Li_2S ($Li_2S - 2e^- \rightarrow 2Li^+ + S$).[22,41] During the second and third scans, two new protruding cathodic peaks appear at 1.94 and 1.25 V, respectively, corresponding to the following two reactions: $2Li^+ + S + 2e^- \rightarrow Li_2S$ and $MoS_2 + xLi^+ + xe^- \rightarrow Li_xMoS_2$, respectively. The cathodic peak at 1.94 V and anodic peak at 2.29 V constitute a reversible redox couple, denoting the sulfide redox reaction. It is proposed that after the first cycle, the electrochemical mechanism of MoS_2 is mainly dominated by the reversible reaction of sulfur to Li_2S.[22,39,40] In addition, the redox peaks of yolk–shell MoS_2@C nanospheres in the second and third cycles are almost overlapped, indicating that the yolk–shell MoS_2@C nanospheres have excellent stability and reversibility, better than those of C@MoS_2 (Figure 6b) and pure MoS_2 (Figure 6c).

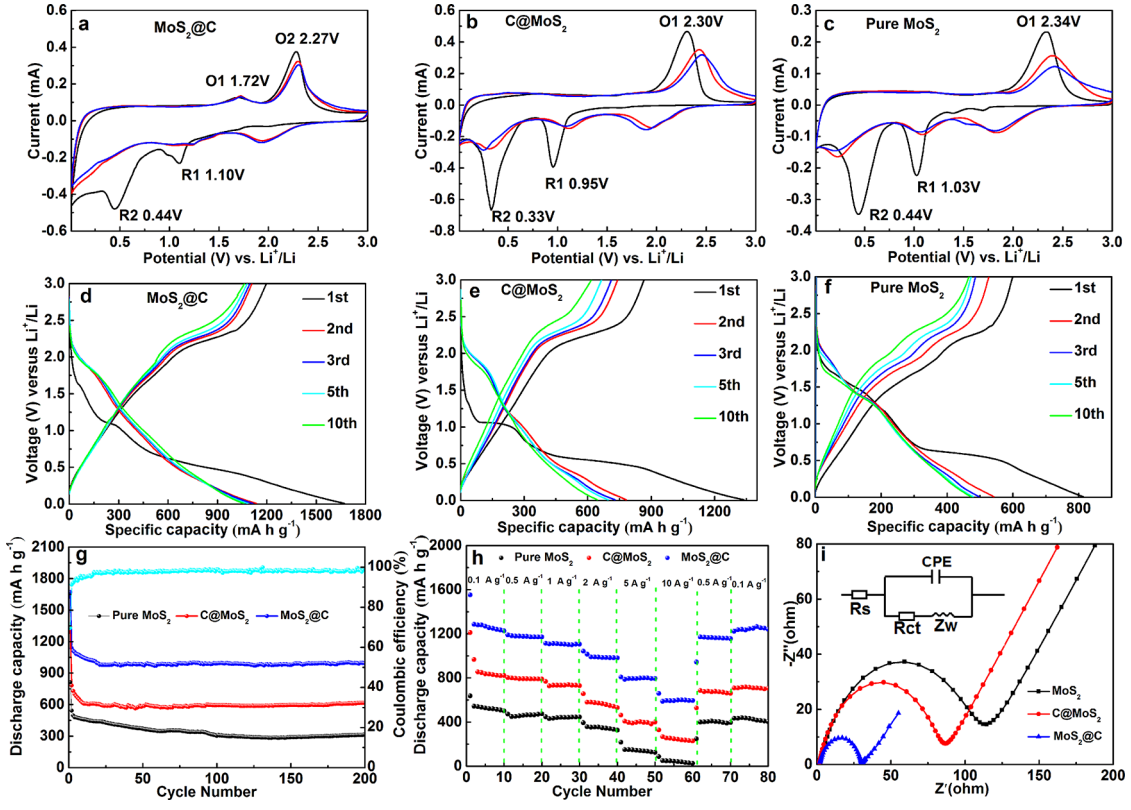

Figure 6. CV profiles of the (a) MoS_2@C, (b) C@MoS_2, and (c) pure MoS_2 over a voltage range of 0.005–3.0 V at a scan rate of 0.1 mV s^{-1}. Charge/discharge voltage profiles of the (d) MoS_2@C, (e) C@MoS_2, and (f) pure MoS_2 at 1 A g^{-1}. (g) Cycling performance of pure MoS_2, C@MoS_2, and MoS_2@C nanospheres and Coulombic efficiency of MoS_2@C nanospheres at 1 A g^{-1}. (h) Cycling performance at various current densities (0.1 to 10 A g^{-1}). (i) Nyquist plots and applied equivalent circuit model (inset).

DOI: 10.1021/acsnano.7b04078
ACS Nano 2017, 11, 8429–8436

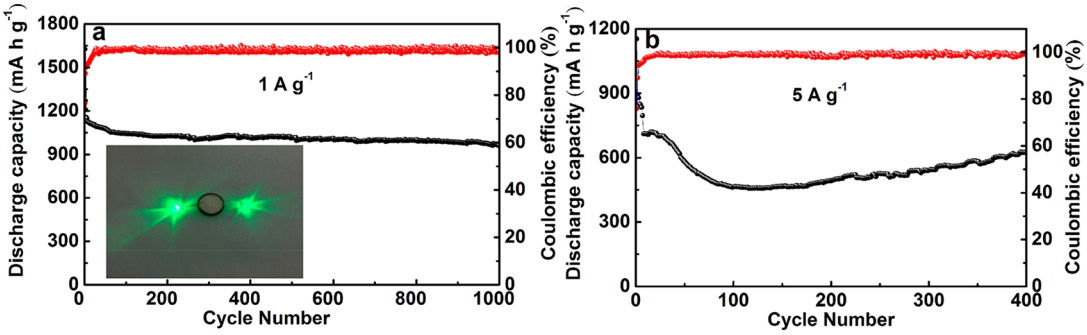

Figure 7. Cycling performance of MoS_2@C nanospheres at (a) 1 A g^{-1} and (b) 5 A g^{-1} (inset: photograph of a LED powered by a coin cell based on the MoS_2@C nanocomposite electrode).

The initial galvanostatic charge/discharge profiles of three electrodes made with MoS_2@C, C@MoS_2, and pure MoS_2, at 1 A g^{-1} current density, are shown in Figure 6d–f. For the first cycle, the discharge and charge capacities of yolk–shell MoS_2@C are 1671 and 1197 mA h g^{-1} (Figure 6d), respectively, higher than those of C@MoS_2 at 1337 and 866 mA h g^{-1} (Figure 6e) and pure MoS_2 at 813 and 580 mA h g^{-1} (Figure 6f), demonstrating that MoS_2@C has the best charge/discharge capacities among the three. This is further supported by the higher Coulombic efficiency (CE) for MoS_2@C at 71.6%, than that of C@MoS_2 at 64.7%. Moreover, after 200 cycles, the yolk–shell MoS_2@C nanospheres maintain high reversible capacities (993 mA h g^{-1}) and cycling stability (almost 100% CE throughout the cycling, in Figure 6g), whereas the discharge capacity of the C@MoS_2 decreases to 618 mA h g^{-1}. The poor reversible capacity of C@MoS_2 may be attributed to the exfoliation of MoS_2 nanosheets from the carbon shell. Pure MoS_2 nanosheets display prompt capacity fade and finally reach 313 mA h g^{-1}. Furthermore, by comparing the electrochemical performance of anodes made of other reported MoS_2-based materials, listed in Table S1, it is clear that our yolk–shell MoS_2@C anode is a highly competitive candidate in terms of capacity output.

The rate performance and the cycling stability of yolk–shell MoS_2@C electrode are compared to C@MoS_2 and pure MoS_2 electrodes in Figure 6h. The discharge capacities of pure MoS_2 nanosheets decrease rapidly at current densities higher than 2 A g^{-1}. The discharge capacities of the C@MoS_2 are 853, 788, 728, 530, 399, and 229 mA h g^{-1} at the current densities of 0.1, 0.5, 1, 2, 5, and 10 A g^{-1}. In contrast, the yolk–shell MoS_2@C nanospheres show much higher specific capacities of 1280, 1170, 1105, 981, 795, and 595 mA h g^{-1}. Furthermore, as the current density returns to 0.5 and then 0.1 A g^{-1}, the discharge capacity of yolk–shell MoS_2@C rapidly resumes to 1155 and 1242 mA h g^{-1}, respectively. Apparently, the rate performance and the cycling stability of yolk–shell MoS_2@C are superior to that of C@MoS_2 and pure MoS_2. The rate performance of yolk–shell MoS_2@C is better than that of the CNT/MoS_2 hybrids and N-doped grapheme/MoS_2.[23,32] Electrochemical impedance spectroscopy (Figure 6i) measurements show that the yolk–shell MoS_2@C nanospheres have the smallest diameter of the high-frequency semicircle among the three, indicating a solid state interface layer resistance lower than that of the pure MoS_2 and C@MoS_2. In addition, the yolk–shell structured MoS_2@C shows outstanding cycling performance at various current densities. At a low current density of 1 A g^{-1} and after 1000 cycles, the discharge capacity of the yolk–shell MoS_2@C nanospheres remains at 962 mA h g^{-1} (Figure 7a). Even at higher current density of 5 A g^{-1}, the yolk–shell MoS_2@C nanospheres still maintain the reversible capacity of 624 mA h g^{-1} after 400 cycles (Figure 7b). A button cell using the yolk–shell MoS_2@C as anode easily powers up the LED lights (3 V, 20 mA) in the inset of Figure 7a, demonstrating an excellent function of yolk–shell MoS_2@C electrode in LIB.

The structure and morphology of the yolk–shell MoS_2@C nanospheres after a cycling performance test were recorded by FESEM, TEM, and EDX mapping (Figure S15 and Figure S16). It is clearly shown that the size, shape, and structural integrity of the carbon skeleton are unchanged. The buffer space provided by voids in yolk–shell MoS_2@C nanospheres, coupled with the confined effect of the carbon shell, allow free expansion/contraction of MoS_2 nanosheets during the lithium-ion intercalation/deintercalation process, resulting in the partial pulverization of MoS_2 structures inside HMCSs. On the contrary, the C@MoS_2 nanospheres suffer from severe volume expansion after a great number of cycles, as evident by the exfoliation of MoS_2 nanosheets from the outer surface of the HMCSs (Figure S17), leading to their poor cycling stability. This demonstrates that the yolk–shell MoS_2@C nanospheres have excellent structural advantage over C@MoS_2.

The superior electrochemical performance of the yolk–shell MoS_2@C nanospheres as an anode material for LIBs can be attributed to the following aspects: (1) High specific surface area (199.2 m^2 g^{-1}) and pore structures of mesoporous carbon shell allow the effective permeation of electrolyte inside HMCSs and bring about a large electrode/electrolyte contact area for Li ion fast diffusion and migration. (2) The yolk–shell structure provides sufficient buffer space for free volume expansion of MoS_2 in lithium ion uptake/release process, preventing the structural exfoliation from carbonaceous materials or current collector. (3) Shell of mesoporous carbon serving as a conductive matrix significantly improves the electrical conductivity of the composite and maintains the integrity structure, ensuring the desired cycling stability and rate performance of electrode material.

CONCLUSIONS

In summary, we have described the rational design and scalable assembly of yolk–shell MoS_2@C nanospheres using HMCSs as nanoreactors. The MoS_2@C nanospheres possess a high specific surface area of 199.2 m^2 g^{-1}, a mesoporous carbon shell, and a well-defined yolk–shell structure. When evaluated as an anode material for LIBs, the yolk–shell MoS_2@C electrode shows a high reversible capacity of 993 mA h g^{-1} at 1 A g^{-1} after 200 cycles, which is a remarkable enhancement in comparison with pure MoS_2 electrode (313 mA h g^{-1}) and the

DOI: 10.1021/acsnano.7b04078
ACS Nano 2017, 11, 8429–8436

C@MoS_2 electrode (618 mA h g^{-1}). Furthermore, the yolk–shell MoS_2@C delivers a superior high-rate capability and retains a reversible capacity of 595 mA h g^{-1} at a current density of 10 A g^{-1}. At various current densities, the yolk–shell MoS_2@C displays the outstanding cycling performance. At 1 A g^{-1} and after 1000 cycles, the discharge capacity of the yolk–shell MoS_2@C nanospheres remains at 962 mA h g^{-1}. The yolk–shell architecture guarantees excellent cycling performance, as well as high capacity and superior rate capability, which are ideal for application in LIBs. This method can be extended to the design and syntheses of other yolk–shell metal dichalcogenide@C nanospheres, such as WS_2@C and SnS_2@C.

EXPERIMENTAL SECTION

Materials. $Na_2MoO_4{\cdot}2H_2O$, thiourea, resorcinol, formaldehyde, $NH_3{\cdot}H_2O$, ethanol, NaOH, and polyvinylidene difluoride (PVDF) were analytical grade and purchased from Shanghai Chemical Corp. The electrolyte solution with 1 M $LiPF_6$/ethylene carbonate (EC)/diethyl carbonate (DEC)/ethyl methyl carbonate (EMC) (1:1:1 by volume) were supplied by Guangzhou Tinci Materials Technology Co., Ltd. Other commercially available chemicals and solvents were reagent grade and used as received.

Synthesis of Hollow Mesoporous Carbon Spheres. Tetraethylorthosilicate and resorcinol formaldehyde oligomers were co-condensed on SiO_2 core particles to form the SiO_2@SiO_2/RF core–shell structured nanospheres. In a typical synthesis of SiO_2@SiO_2/RF, 3.46 mL of TEOS was added to the solution containing 70 mL of ethanol, 10 mL of H_2O, and 3 mL of ammonia solution (25 wt %) under vigorous stirring at room temperature. After 15 min, 0.4 g of resorcinol and 0.56 mL of formaldehyde (37 wt %) were added to the solution, and the system was kept under vigorous stirring for 24 h at room temperature. The precipitates were separated by centrifugation, washed with deionized water and ethanol, and then dried at 60 °C overnight. Second, the precipitates were calcinated under N_2 to 700 °C (2 °C min^{-1}) for 5 h to obtain the SiO_2@SiO_2/C nanospheres. Finally, HMCSs with a 20 nm thick carbon shell were obtained by removing silica using sodium hydroxide (NaOH, 1 M).

Tetrapropylorthosilicate, instead of TEOS, was used to for the synthesis of hollow mesoporous carbon spheres with a 65 nm thick carbon shell.

Synthesis of Yolk–Shell MoS_2@C Nanospheres. First, 0.5 g of $Na_2MoO_4{\cdot}2H_2O$ and 1.0 g of $CS(NH_2)_2$ were dissolved into 30 mL of deionized water to form a transparent solution under ultrasonic dispersion for 30 min, followed by dissolving 100 mg of HMCSs into the solution. After ultrasonic dispersion for 50 min, the black solution was transferred to a 60 mL Teflon-lined stainless-steel autoclave. The autoclave was then heated in an air-flow electric oven at 200 °C for 24 h. After that, the autoclave was cooled to room temperature. The solution was transferred out for centrifugation. The black particles were collected and washed six times with deionized water and ethanol before being dried at 60 °C in vacuum overnight. Then the product was calcined in a tube furnace at 800 °C for 2 h under Ar atmosphere to obtain yolk–shell MoS_2@C nanospheres.

Synthesis of C@MoS_2 Nanospheres. The obtained 100 mg of SiO_2@SiO_2/C nanospheres of intermediate products of HMCSs was dissolved in 30 mL of deionized water containing $Na_2MoO_4{\cdot}2H_2O$ (0.5 g) and $CS(NH_2)_2$ (1.0 g) solution, stirred for 30 min, and transferred into a 60 mL Teflon-lined autoclave and heated at 200 °C for 24 h. After being cooled to room temperature, the precipitates were washed with deionized water and ethanol several times. Then the precipitates were dried at 60 °C for 12 h. The dried powder was etched by 1 M NaOH and calcined in a tube furnace at 800 °C for 2 h under argon.

Synthesis of Pure MoS_2 Nanosheets. $Na_2MoO_4{\cdot}2H_2O$ (0.5 g) and $CS(NH_2)_2$ (1.0 g) were dissolved in 30 mL of deionized water under continuous stirring for 30 min to form a homogeneous solution. Then, the mixture was transferred into a 60 mL Teflon-lined stainless-steel autoclave and kept at 200 °C for 24 h. Then, the precipitates were separated by centrifugation, washed with deionized water and ethanol, and dried at 60 °C for 12 h. Finally, the product was calcined at 800 °C for 2 h under argon.

Materials Characterization. Field-emission scanning electron microscopy was carried out with a Hitachi S-4800 microscope (Japan). Transmission electron microscopy was conducted on a Philips TECNAI-12 instrument. High-resolution TEM and high-angle annular dark-field scanning transmission electron microscopy were performed on a FEI Tecnai G2 F30 STWIN (USA) operating at 300 kV. X-ray diffraction data were obtained on a D8 advance superspeed powder diffractometer (Bruker). Raman spectra were carried out on Renishaw Invia Raman spectroscope. X-ray photoelectron spectroscopy was conducted with a Thermo Escalab 250 system. Surface areas and pore size distributions were recorded by BET technique in an automated surface area and porosity analyzer (ASAP 2020, HD88) at −196 °C after samples were dried at 100 °C for 4 h.

Electrochemical Tests. Anode electrodes were prepared by mixing the yolk–shell MoS_2@C nanospheres (80%) with 10% acetylene black as a conductive material and 10% PVDF binder dissolved in *N*-methyl-2-pyrrolidinone. Then, the slurries were cast onto a copper foil current collector. After being coated, the electrodes were dried at 80 °C for 10 h to remove the solvent before being pressed. The electrodes were punched in the form of disks and then vacuum-dried at 120 °C for 12 h. Then, the button cells (CR 2032 coin-type cell) were assembled with metallic lithium as the counter/reference electrode, 1 M $LiPF_6$ in EC/DEC/EMC (1:1:1 by volume) as electrolyte, and Celgard 2400 polypropylene as separator in a high-purity argon-filled glovebox (Vacuum Atmospheres Co., Ltd.).

Cyclic voltammetry measurements were performed using an electrochemical workstation (CHI660 E, Chenghua, CHN) at a scan rate of 0.1 mV s^{-1} between 0.005 and 3.0 V. Electrochemical impedance spectroscopic experiments were performed with Autolab electrochemical analyzer (Ecochemie, The Netherlands). Galvanostatic charge (lithium insertion) and discharge (lithium extraction) cycling of the cells were carried out using a battery test system (CT-3008W, Xinwei, CHN) at the various current densities between 0.005 and 3 V (*vs* Li^+/Li) to determine ratio performance and to evaluate cycle stability at the current density of 1 A g^{-1}.

ASSOCIATED CONTENT

Supporting Information

The Supporting Information is available free of charge on the ACS Publications website at DOI: 10.1021/acsnano.7b04078.

Additional information for the characterization of samples and the electrochemical data (PDF)

AUTHOR INFORMATION

Corresponding Authors

*E-mail: chenming@yzu.edu.cn.

*E-mail: gwdiao@yzu.edu.cn.

ORCID

Guowang Diao: 0000-0001-9224-5432

Ming Chen: 0000-0002-6436-4765

Notes

The authors declare no competing financial interest.

ACKNOWLEDGMENTS

This work was financially supported by the National Natural Science Foundation of China (Grant No. 21511140282), Natural Science Foundation of Jiangsu Province (BK20161329), and a Project Funded by the Priority Academic Program Development of Jiangsu Higher Education Institutions. The work was also sponsored by Qing Lan Project of Higher Learning Institutions in Jiangsu Province, the support of high-end talent plan of Yangzhou University, and supported by

DOI: 10.1021/acsnano.7b04078
ACS Nano 2017, 11, 8429–8436

Jiangsu Key Laboratory of Advanced Catalytic Materials and Technology (JLCT201702).

REFERENCES

(1) Mo, R. W.; Rooney, D.; Sun, K. N.; Yang, H. Y. 3D Nitrogen-Doped Graphene Foam with Encapsulated Germanium/Nitrogen-Doped Graphene Yolk-Shell Nanoarchitecture for High-Performance Flexible Li-Ion Battery. *Nat. Commun.* **2017**, *8*, 13949.

(2) Hu, H.; Guan, B. Y.; Xia, B. Y.; Lou, X. W. Designed Formation of $Co_3O_4/NiCo_2O_4$ Double-Shelled Nanocages with Enhanced Pseudocapacitive and Electrocatalytic Properties. *J. Am. Chem. Soc.* **2015**, *137*, 5590−5595.

(3) Wu, C.; Kopold, P.; van Aken, P. A.; Maier, J.; Yu, Y. High Performance Graphene/Ni_2P Hybrid Anodes for Lithium and Sodium Storage through 3D Yolk-Shell-Like Nanostructural Design. *Adv. Mater.* **2017**, *29*, 1604015.

(4) Liu, J.; Qiao, S. Z.; Chen, J. S.; Lou, X. W.; Xing, X. R.; Lu, G. Q. Yolk/Shell Nanoparticles: New Platforms for Nanoreactors, Drug Felivery and Lithium-Ion Batteries. *Chem. Commun.* **2011**, *47*, 12578−12591.

(5) Lee, I.; Joo, J. B.; Yin, Y. D.; Zaera, F. A Yolk@Shell Nanoarchitecture for Au/TiO_2 Catalysts. *Angew. Chem., Int. Ed.* **2011**, *50*, 10208−10211.

(6) Wu, S.; Dzubiella, J.; Kaiser, J.; Drechsler, M.; Guo, X. H.; Ballauff, M.; Lu, Y. Thermosensitive Au-PNIPA Yolk-Shell Nanoparticles with Tunable Selectivity for Catalysis. *Angew. Chem., Int. Ed.* **2012**, *51*, 2229−2233.

(7) Yang, J. P.; Shen, D. K.; Zhou, L.; Li, W.; Li, X. M.; Yao, C.; Wang, R.; El-Toni, A. M.; Zhang, F.; Zhao, D. Y. Spatially Confined Fabrication of Core-Shell Gold Nanocages@Mesoporous Silica for Near-Infrared Controlled Photothermal Drug Release. *Chem. Mater.* **2013**, *25*, 3030−3037.

(8) Liu, J.; Qiao, S. Z.; Budi Hartono, S.; Lu, G. Q. Monodisperse Yolk-Shell Nanoparticles with a Hierarchical Porous Structure for Delivery Vehicles and Nanoreactors. *Angew. Chem., Int. Ed.* **2010**, *49*, 4981−4985.

(9) Gao, J. H.; Liang, G. L.; Cheung, J. S.; Pan, Y.; Kuang, Y.; Zhao, F.; Zhang, B.; Zhang, X. X.; Wu, E. X.; Xu, B. Multifunctional Yolk-Shell Nanoparticles: A Potential MRI Contrast and Anticancer Agent. *J. Am. Chem. Soc.* **2008**, *130*, 11828−11833.

(10) Liu, N.; Wu, H.; McDowell, M. T.; Yao, Y.; Wang, C. M.; Cui, Y. A Yolk-Shell Design for Stabilized and Scalable Li-Ion Battery Alloy Anodes. *Nano Lett.* **2012**, *12*, 3315−3321.

(11) Seh, Z. W.; Li, W. Y.; Cha, J. J.; Zheng, G. Y.; Yang, Y.; McDowell, M. T.; Hsu, P. C.; Cui, Y. Sulphur-TiO_2 Yolk-Shell Nanoarchitecture with Internal Void Space for Long-Cycle Lithium-Sulphur Batteries. *Nat. Commun.* **2013**, *4*, 1331.

(12) Hong, Y. J.; Son, M. Y.; Kang, Y. C. One-Pot Facile Synthesis of Double-Shelled SnO_2 Yolk-Shell-Structured Powders by Continuous Process as Anode Materials for Li-Ion Batteries. *Adv. Mater.* **2013**, *25*, 2279−2283.

(13) Zhang, H. W.; Zhou, L.; Noonan, O.; Martin, D. J.; Whittaker, A. K.; Yu, C. Z. Tailoring the Void Size of Iron Oxide@Carbon Yolk-Shell Structure for Optimized Lithium Storage. *Adv. Funct. Mater.* **2014**, *24*, 4337−4342.

(14) Wu, X. J.; Xu, D. S. Soft Template Synthesis of Yolk/Silica Shell Particles. *Adv. Mater.* **2010**, *22*, 1516−1520.

(15) Yu, L.; Guan, B. Y.; Xiao, W.; Lou, X. W. Formation of Yolk-Shelled Ni-Co Mixed Oxide Nanoprisms with Enhanced Electrochemical Performance for Hybrid Supercapacitors and Lithium Ion Batteries. *Adv. Energy Mater.* **2015**, *5*, 1500981.

(16) Gao, J. H.; Liang, G. L.; Zhang, B.; Kuang, Y.; Zhang, X. X.; Xu, B. FePt@CoS_2 Yolk-Shell Nanocrystals as a Potent Agent to Kill HeLa Cells. *J. Am. Chem. Soc.* **2007**, *129*, 1428−1433.

(17) Hong, Y. J.; Son, M. Y.; Park, B. K.; Kang, Y. C. One-Pot Synthesis of Yolk-Shell Materials with Single, Binary, Ternary, Quaternary, and Quinary Systems. *Small* **2013**, *9*, 2224−2227.

(18) Zhang, Q.; Lee, I.; Ge, J. P.; Zaera, F.; Yin, Y. D. Surface-Protected Etching of Mesoporous Oxide Shells for the Stabilization of Metal Nanocatalysts. *Adv. Funct. Mater.* **2010**, *20*, 2201−2214.

(19) Joo, J. B.; Liu, H. Y.; Lee, Y. J.; Dahl, M.; Yu, H. X.; Zaera, F.; Yin, Y. D. Tailored Synthesis of C@TiO_2 Yolk-Shell Nanostructures for Highly Efficient Photocatalysis. *Catal. Today* **2016**, *264*, 261−269.

(20) Zhang, L.; Wu, H. B.; Yan, Y.; Wang, X.; Lou, X. W. Hierarchical MoS_2 Microboxes Constructed by Nanosheets with Enhanced Electrochemical Properties for Lithium Storage and Water Splitting. *Energy Environ. Sci.* **2014**, *7*, 3302−3306.

(21) Zhou, W. J.; Yin, Z. Y.; Du, Y. P.; Huang, X.; Zeng, Z. Y.; Fan, Z. X.; Liu, H.; Wang, J. Y.; Zhang, H. Synthesis of Few-Layer MoS_2 Nanosheet-Coated TiO_2 Nanobelt Heterostructures for Enhanced Photocatalytic Activities. *Small* **2013**, *9*, 140−147.

(22) Chang, K.; Geng, D. S.; Li, X. F.; Yang, J. L.; Tang, Y. J.; Cai, M.; Li, R. Y.; Sun, X. L. Ultrathin MoS_2/Nitrogen-Doped Graphene Nanosheets with Highly Reversible Lithium Storage. *Adv. Energy. Mater.* **2013**, *3*, 839−844.

(23) Shan, T. T.; Xin, S.; You, Y.; Cong, H. P.; Yu, S. H.; Manthiram, A. Combining Nitrogen-Doped Graphene Sheets and MoS_2: A Unique Film-Foam-Film Structure for Enhanced Lithium Storage. *Angew. Chem., Int. Ed.* **2016**, *55*, 12783−12788.

(24) Wang, Y. S.; Ma, Z. M.; Chen, Y. J.; Zou, M. C.; Yousaf, M.; Yang, Y. B.; Yang, L. S.; Cao, A. Y.; Han, R. P. S. Controlled Synthesis of Core-Shell Carbon@MoS_2 Nanotube Sponges as High-Performance Battery Electrodes. *Adv. Mater.* **2016**, *28*, 10175−10181.

(25) Xia, Y.; Wang, B. B.; Zhao, X. J.; Wang, G.; Wang, H. Core-Shell Composite of Hierarchical MoS_2 Nanosheets Supported on Graphitized Hollow Carbon Microspheres for High Performance Lithium-Ion Batteries. *Electrochim. Acta* **2016**, *187*, 55−64.

(26) Wan, Z. M.; Shao, J.; Yun, J. J.; Zheng, H. Y.; Gao, T.; Shen, M.; Qu, Q. T.; Zheng, H. H. Core-Shell Structure of Hierarchical Quasi-Hollow MoS_2 Microspheres Encapsulated Porous Carbon as Stable Anode for Li-Ion Batteries. *Small* **2014**, *10*, 4975−4981.

(27) Li, H. S.; Wang, X. Y.; Ding, B.; Pang, G.; Nie, P.; Shen, L. F.; Zhang, X. G. Enhanced Lithium-Storage Performance from Three-Dimensional MoS_2 Nanosheets/Carbon Nanotube Paper. *ChemElectroChem* **2014**, *1*, 1118−1125.

(28) Chen, G.; Wang, S. P.; Yi, R.; Tan, L. F.; Li, H. B.; Zhou, M.; Yan, L. T.; Jiang, Y. B.; Tan, S.; Wang, D. H.; et al. Facile Synthesis of Hierarchical MoS_2-Carbon Microspheres as a Robust Anode for Lithium Ion Batteries. *J. Mater. Chem. A* **2016**, *4*, 9653−9660.

(29) Cui, C. Y.; Li, X.; Hu, Z.; Xu, J. T.; Liu, H. K.; Ma, J. M. Growth of MoS_2@C Nanobowls as a Lithium-Ion Battery Anode Material. *RSC Adv.* **2015**, *5*, 92506−92514.

(30) Bai, Z. C.; Zhang, Y. H.; Zhang, Y. W.; Guo, C. L.; Tang, B. Hierarchical MoS_2@Carbon Microspheres as Advanced Anodes for Li-Ion Batteries. *Chem. - Eur. J.* **2015**, *21*, 18187−18191.

(31) Zhang, L.; Lou, X. W. Hierarchical MoS_2 Shells Supported on Carbon Spheres for Highly Reversible Lithium Storage. *Chem. - Eur. J.* **2014**, *20*, 5219−5223.

(32) Chen, Y. M.; Yu, X. Y.; Li, Z.; Paik, U.; Lou, X. W. Hierarchical MoS_2 Tubular Structures Internally Wired by Carbon Nanotubes as a Highly Stable Anode Material for Lithium-Ion Batteries. *Sci. Adv.* **2016**, *2*, e1600021.

(33) Sun, Z.; Yao, Y. C.; Wang, J.; Song, X. F.; Zhang, P.; Zhao, L. P.; Gao, L. High Rate Lithium-Ion Batteries from Hybrid Hollow Spheres with a Few-Layered MoS_2-Entrapped Carbon Sheath Synthesized by a Space-Confined Reaction. *J. Mater. Chem. A* **2016**, *4*, 10425−10434.

(34) Li, G. D.; Zeng, X. Y.; Zhang, T. D.; Ma, W. Y.; Li, W. P.; Wang, M. Facile Synthesis of Hierarchical Hollow MoS_2 Nanotubes as Anode Materials for High-Performance Lithium-Ion Batteries. *CrystEngComm* **2014**, *16*, 10754−10759.

(35) Fuertes, A. B.; Valle-Vigon, P.; Sevilla, M. One-Step Synthesis of Silica@Resorcinol-Formaldehyde Spheres and Their Application for the Fabrication of Polymer and Carbon Capsules. *Chem. Commun.* **2012**, *48*, 6124−6126.

(36) Zhang, H. W.; Noonan, O.; Huang, X. D.; Yang, Y. N.; Xu, C.; Zhou, L.; Yu, C. Z. Surfactant-Free Assembly of Mesoporous Carbon

DOI: 10.1021/acsnano.7b04078
ACS Nano 2017, 11, 8429−8436

Hollow Spheres with Large Tunable Pore Sizes. *ACS Nano* **2016**, *10*, 4579−4586.
(37) Chang, K.; Chen, W. X. L-Cysteine-Assisted Synthesis of Layered MoS_2/Graphene Composites with Excellent Electrochemical Performances for Lithium Ion Batteries. *ACS Nano* **2011**, *5*, 4720−4728.
(38) Wang, J.; Liu, J. L.; Chao, D. L.; Yan, J. X.; Lin, J. Y.; Shen, Z. X. Self-Assembly of Honeycomb-Like MoS_2 Nanoarchitectures Anchored into Graphene Foam for Enhanced Lithium-Ion Storage. *Adv. Mater.* **2014**, *26*, 7162−7169.
(39) Stephenson, T.; Li, Z.; Olsen, B.; Mitlin, D. Lithium Ion Battery Applications of Molybdenum Disulfide (MoS_2) Nanocomposites. *Energy Environ. Sci.* **2014**, *7*, 209−231.
(40) Chang, K.; Chen, W. *In Situ* Synthesis of MoS_2/Graphene Nanosheet Composites with Extraordinarily High Electrochemical Performance for Lithium Ion Batteries. *Chem. Commun.* **2011**, *47*, 4252−4254.
(41) Zhu, C.; Mu, X.; van Aken, P. A.; Yu, Y.; Maier, J. Single-Layered Ultrasmall Nanoplates of MoS_2 Embedded in Carbon Nanofibers with Excellent Electrochemical Performance for Lithium and Sodium Storage. *Angew. Chem., Int. Ed.* **2014**, *53*, 2152−2156.

DOI: 10.1021/acsnano.7b04078
ACS Nano 2017, 11, 8429−8436